ACS NANO

www.acsnano.org

ARTICLE

Coupling of Nondegenerate Topological Modes in Nitrogen Core-Doped Graphene Nanoribbons

Peter H. Jacobse,▲ Michele Pizzochero,▲ Ethan Chi Ho Wen,▲ Gabriela Borin Barin, Xinheng Li, Zafer Mutlu, Klaus Müllen, Efthimios Kaxiras, Michael F. Crommie,* and Felix R. Fischer*

Cite This: *ACS Nano* 2025, 19, 13029−13036

Read Online

ACCESS | Metrics & More | Article Recommendations | Supporting Information

ABSTRACT: **Nitrogen core-doping of graphene nanoribbons (GNRs) allows trigonal planar carbon atoms along the backbone of GNRs to be substituted by higher-valency nitrogen atoms. The excess valence electrons are injected into the π-orbital system of the GNR, thereby changing not only its electronic occupation but also its topological properties. We have observed this topological change by synthesizing dilute nitrogen core-doped armchair GNRs with a width of five atoms (N_2-5-AGNRs). The incorporation of pairs of trigonal planar nitrogen atoms results in the emergence of topological boundary states at the interface between doped and undoped segments of the GNR. These topological boundary states are offset in energy by approximately ΔE = 300 meV relative to the topological end states at the termini of finite 5-AGNRs. Scanning tunneling microscopy (STM) and spectroscopy (STS) reveal that for finite GNRs the two types of topological states can interact through a linear combination of orbitals, resulting in a pair of asymmetric hybridized states. This behavior is captured by an effective Hamiltonian of nondegenerate diatomic molecules, where the analogous interatomic hybridization interaction strength is tuned by the distance between GNR topological modes.**

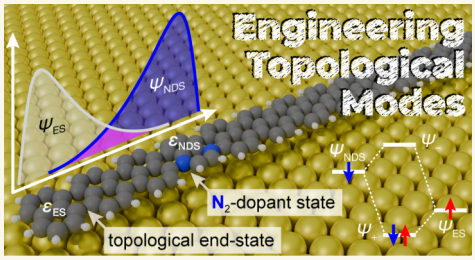

KEYWORDS: *graphene nanoribbons, topological modes, nitrogen core-doping, hybridization, end states, zero mode engineering*

INTRODUCTION

Bottom-up synthesized graphene nanoribbons (GNRs) have emerged as testbeds for realizing simple quantum systems due to extensive opportunities to engineer their electronic structure and the ease of creating new localized states within band gaps.[1−10] Such localized states have been used as basis states in effective low-energy designer Hamiltonians. For example, junctions between 7-, 9-, and 11-atom wide segments of armchair-type GNRs (AGNRs) induce zero-modes that can be coupled to form dimers, oligomers, or superlattices.[11−17] The low-energy physics of these systems can be captured by effective Hamiltonians such as the Su-Schrieffer-Heeger model, the Hubbard dimer model, or the Heisenberg model.[18−21] GNRs with coupled localized modes may similarly be thought of as emulating simple Hamiltonians commonly found in molecular structures, e.g., the extended π-system of conjugated polyenes and aromatics rings.[22−24] The ability to tune the coupling between localized modes (i.e., the hopping interaction, t, in tight-binding models) by changing structural parameters such as intermode separation or nanoribbon structure permits the exploration of effective Hamiltonians over a wide parameter space.[25−30]

One type of Hamiltonian that has not yet been emulated successfully within the framework of GNRs involves coupling nondegenerate localized states akin to the polarized bonding picture in heteronuclear diatomic molecules (e.g., CO).[31] Effective Hamiltonians of this sort with staggered basis state energies have not yet been studied systematically in the context of GNRs. This represents an important omission because staggered-mode quantum systems have profound technological implications. For example, resonant tunneling diodes have a staggered potential profile where electrostatic shifting in the forward direction induces degeneracy and the creation of a resonant tunneling pathway.[32−36] The offset in frontier states between donor−acceptor groups in molecules is also central to the working principles of charge-transfer materials such as

Received: December 5, 2024
Revised: March 18, 2025
Accepted: March 19, 2025
Published: March 27, 2025

organic photovoltaics and Aviram-Ratner molecular diodes.[37−42]

Here we explore this type of behavior in GNRs by utilizing localized nondegenerate topological boundary modes. We exploit the fact that the surplus electrons provided by nitrogen doping in N_2-5-AGNRs induce a topological change from *nontrivial* (i.e., $\mathbb{Z}_2 = 1$, where $\mathbb{Z}_2$ is the topological invariant related to the Zak phase) to *trivial* (i.e., $\mathbb{Z}_2 = 0$).[43] Previously this was used to manipulate end states,[43] but here we show that N-doping can also be used to create *internal* boundary modes that can be exploited as basis states for effective Hamiltonians.

We accomplish this by synthesizing dilute nitrogen core-doped 5-AGNRs and studying their electronic structure via scanning tunneling microscopy (STM) and spectroscopy (STS). We find that nitrogen-induced topological modes, herein referred to as nitrogen dopant states (NDSs), project from quinoxaline units inside 5-AGNRs; the observation is reminiscent of boron-induced topological boundary states in 7-AGNRs.[4,23] Isolated NDSs are energetically offset relative to the topological end states (ESs) of pristine 5-AGNRs: NDSs are observed at $\varepsilon_{NDS} = 400$ meV while ESs reside at $\varepsilon_{ES} = 100$ meV. The distance-dependent hybridization between NDSs and ESs in finite-sized 5-AGNRs results in polarized bonding and antibonding states akin to the π and π^* orbitals of a C═O group in a diatomic molecular picture. Our topological GNR system is effectively described by a two-site Hamiltonian with tunable interaction strength and staggered on-site energies wherein the energy levels trace out an avoided crossing.

It is useful to first discuss the generic two-site tight-binding (TB) model with basis state energies ε_{NDS} and ε_{ES} coupled through a hopping interaction t. The basis states, whose wave functions ψ_{NDS} and ψ_{ES} are shown schematically at the top of Figure 1A, experience an effective interaction as a result of the overlap of their wave functions.[44] The Hamiltonian of this system can then be written as

$$\mathbf{H} = \begin{pmatrix} \varepsilon_{NDS} & t \\ t & \varepsilon_{ES} \end{pmatrix} = \langle\varepsilon\rangle\mathbf{I} + \begin{pmatrix} \Delta\varepsilon/2 & t \\ t & -\Delta\varepsilon/2 \end{pmatrix} \quad (1)$$

where $\langle\varepsilon\rangle = (\varepsilon_{NDS} + \varepsilon_{ES})/2$ is the average energy of the basis states and $\Delta\varepsilon = (\varepsilon_{NDS} - \varepsilon_{ES})$. As illustrated in Figure 1A, the eigenenergies of this Hamiltonian are $\varepsilon_{\pm} = \langle\varepsilon\rangle \pm t_{eff}$, with the + (−) solution denoting the bonding (antibonding) eigenstate and

$$t_{eff} = \sqrt{\left(\frac{\Delta\varepsilon}{2}\right)^2 + t^2} = \left|t + i\frac{\Delta\varepsilon}{2}\right| \quad (2)$$

is the effective hybridization interaction between the two basis states.[31,45] Equation 2 suggests that when the interaction strength t is tuned over a continuous range of values from negative (bonding) to positive (antibonding), the eigenstate energies trace out the branches of a hyperbola (Figure 1B). For vanishing offset $\Delta\varepsilon$ the eigenvalues become degenerate at $t = 0$ but any nonzero value of $\Delta\varepsilon$ induces an avoided crossing gap of magnitude $\Delta E_{(t=0)} = \Delta\varepsilon$. The resulting hyperbolae $E(t)$ can be interpreted as conic sections in three-dimensional (t, $\Delta\varepsilon$, E)-space where the eigenenergy offset $\Delta\varepsilon$ shifts the interaction away from the cone intersection (inset in Figure 1B).

An energy level diagram for the TB model (Figure 1C) shows how new eigenstate energies ε_+ and ε_- are distributed around the average energy $\langle\varepsilon\rangle$ by an amount $\pm t_{eff}$. The various wave functions are shown as plots of $\psi(x)$ and as orbitals

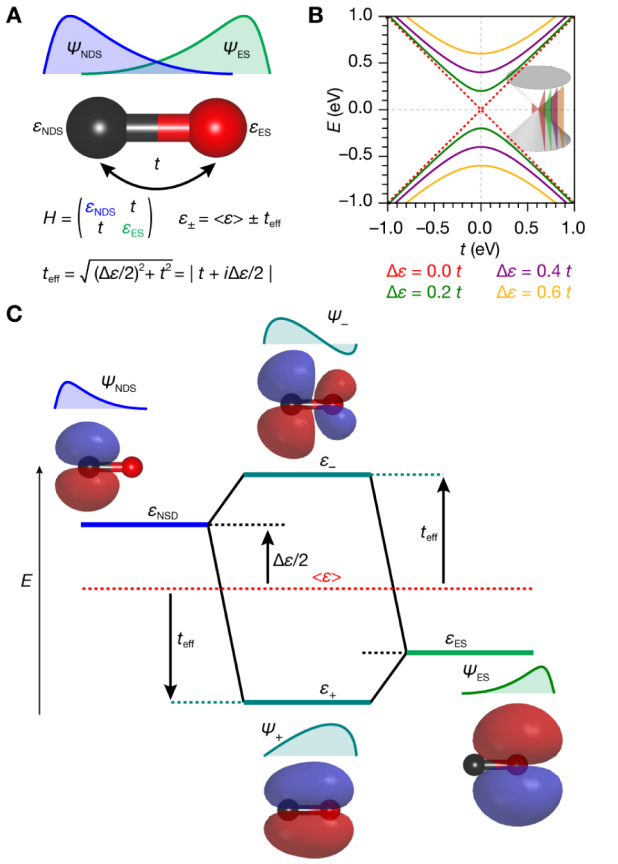

Figure 1. (A) Schematic representation of the nitrogen dopant state wave function ψ_{NDS} and end state wave function ψ_{ES} and their overlap; two-site tight binding model with coupling t between the basis states; Hamiltonian matrix and eigenenergies. (B) Energy level diagram of the eigenenergies ε_+ (bottom branch) and ε_- (top branch) as a function of their interaction t for various values of $\Delta\varepsilon$. Inset shows hyperbolae as conic sections in (t, $\Delta\varepsilon$, E)-space. (C) Energy level diagram showing the basis state energies (ε_{NDS}, ε_{ES}) and hybridized state energies (ε_-, ε_+). Schematic representations of ψ_{NDS}, ψ_{ES}, ψ_+, ψ_-, and the corresponding molecular orbitals for a diatomic model.

models in the insets to Figure 1C. ψ_+ and ψ_- are polarized, with the wave function of the bonding state having larger contributions from the lower-energy basis state ψ_{ES}, while the antibonding state is dominated by the contribution from ψ_{NSD}. This is reminiscent of the familiar orbital picture for hetero diatomic molecules (e.g., the polarized π-bond in C═O) and donor−acceptor molecules.[46] By analogy, the NDS may be interpreted as a π-bonding (donor) state and the ES as a π^*-antibonding (acceptor) state.

In the context of the dilute N-doped 5-AGNRs studied here, the ES represents the native topological state of the undoped 5-AGNR while the NDS is a topological state of a N_2-5-AGNR whose Fermi level (E_F) is upshifted relative to the E_F of a pristine 5-AGNR. Since these topological states lie near the midgap energy of their respective GNRs, a significant energy offset exists between the NDS and ES. The length of the 5-AGNR segment separating the NDS tunes the strength of the hybridization interaction between these nondegenerate topological modes and allows us to emulate the dimer Hamiltonian shown in Figure 1 for a range of t values (see Supporting Information Discussion 1 and Figure S1).

https://doi.org/10.1021/acsnano.4c17602
ACS Nano 2025, 19, 13029−13036

RESULTS AND DISCUSSION

Dilute N_2-5-AGNRs were synthesized through on-surface copolymerization of 5,8-di(1-iodo-4-naphthyl)quinoxaline (DINQ; the precursor for N_2-5-AGNRs)[43] and a mixture of 3,9-diiodoperylene and 3,10-diiodoperylene (DIP; the precursor molecules for undoped 5-AGNRs)[47] at a surface ratio of 1:9 (Figure 2A). Sequential deposition of DINQ and DIP from

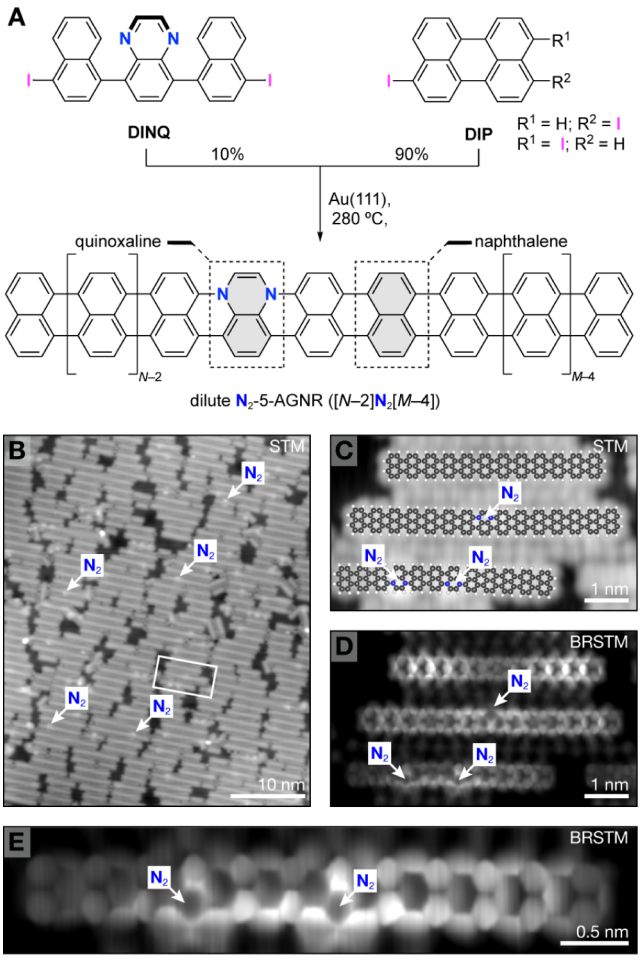

Figure 2. (A) On-surface synthesis of dilute doped N_2-5-AGNRs from precursors DINQ and DIP. (B) STM topographic image (V_s = −200 mV, I = 60 pA) of dilute doped N_2-5-AGNRs. (C) STM topographic image (V_s = −100 mV, I = 100 pA) of three laterally aligned GNRs. (D) BRSTM image (tunneling current I at V_s = 200 mV) of the three GNRs in (C). (E) BRSTM image (tunneling current I at V_s = 100 mV) recorded on the bottom GNR in (D). The positions of quinoxaline units are indicated by arrows.

a home-built Knudsen cell onto a clean Au(111) surface followed by annealing to T = 120 °C for t = 30 min, and subsequently to T = 280 °C for t = 15 min yielded samples of dilute doped N_2-5-AGNRs (Figure S2). Figure 2B shows a representative topographic STM image of aligned 5-AGNRs with lengths ranging from 2 nm < l < 15 nm. Residual iodine atoms line the spaces between ribbons (moderate annealing temperatures are critical to prevent cross-linking of GNRs but insufficient to ensure the complete desorption of halogen atoms). Bright protrusions (see arrows) correspond to isolated nitrogen-doped quinoxaline units embedded along the backbone of otherwise all-carbon 5-AGNRs.

Figure 2C shows a topographic STM image of three parallel GNRs highlighted in Figure 2B (structural model is overlaid). BRSTM (Figure 2D,E) using CO functionalized tips[48] resolves all 6-membered rings in the GNR backbone. The top GNR in Figure 2D can be readily identified as a pristine 5-AGNR with N = 12 repeating naphthalene units (referred to as 5-AGNR(12)). The middle GNR features N = 15 repeating units but the eighth unit has a distinctly different appearance with one of the rings exhibiting a notably darker contrast along the edge (indicated by an arrow in Figure 2D, see Figure S3 for Laplace filtered images). This is consistent with previous observations of nitrogen core-doped 5-AGNRs where quinoxaline units were consistently imaged with reduced contrast in BRSTM.[43] We herein label this ribbon 5-AGNR($7N_27$) (i.e., one central quinoxaline unit flanked on either side by two segments of N = 7 naphthalene units). The third GNR exhibiting two darker rings in BRSTM (Figure 2E) can then be identified as 5-AGNR($3N_22N_25$).

End States and Nitrogen Dopant States. Figure 3A shows an STM topographic image of a 5-AGNR(14) and a 5-AGNR($11N_23$) (structural models are overlaid). STS spectra were recorded along the length of both GNRs (dashed yellow arrows in Figure 3A). Differential conductance $dI/dV(V_s, x)$ spectra recorded as a function of sample bias V_s and position x along the length of the undoped 5-AGNR(14) are depicted in Figure 3B. The spectra clearly show a valence band (VB) onset at $V_s \approx -400$ mV, a conduction band (CB) onset at $V_s \approx 800$ mV, along with the characteristic signatures of 5-AGNR ESs at both ends of the GNR at $V_s \approx 100$ mV; consistent with previous work on undoped 5-AGNRs.[49] The same features can be recognized in dI/dV point spectra recorded at the center (red) of the 5-AGNR(14) and at the left end (green) in Figure 3C.

STS acquired with the same tip on the adjacent N-doped 5-AGNR($11N_23$) shows the expected VB and CB onsets at $V_s \approx -400$ mV and $V_s \approx 800$ mV, and an ES at $V_s \approx 100$ mV for the left end of the ribbon (Figure 3D). The ES on the right side, however, is not observed. Instead, an intense localized spectroscopic feature is seen at $x \approx 5$ nm (the position of the quinoxaline) that extends energetically into the bandgap and a new weaker feature at $V_s \approx 400$ mV that extends spatially for more than 1 nm to the left of the quinoxaline unit (NDS in Figure 3D). Point spectra (Figure 3E) acquired at the center (red) and left end (green) of the 5-AGNR($11N_23$) reveal the VB and CB onsets and an ES at V_s = 107 mV (Figure 3E). The new NDS state is observed as a peak at V_s = 431 mV (Gaussian fit) in a point spectrum acquired to the left of the quinoxaline unit (dashed blue line in Figure 3E). Constant height dI/dV maps (using CO-functionalized tips) recorded at the CB and VB onsets (V_s = 800 mV and V_s = −400 mV, Figure 3F,J) reveal wave function patterns that are consistent with bulk 5-AGNR states.[49] The map recorded at energies corresponding to the ES (V_s = 100 mV, Figure 3H) shows orbital density on both sides for the 5-AGNR but only on the left side of the 5-AGNR($11N_23$). The signal maximum for the ES is centered on the second and third last naphthalene units, respectively, before gradually decaying toward the vacuum interface (this is to avoid a discontinuity in the wave function at the GNR/vacuum interface). A map acquired at V_s = 400 mV (Figure 3G) shows that the NDS has a similar appearance to an ES. Its maximum however is localized at the interface between 5-AGNR and the quinoxaline unit decaying over the distance of ∼ 1 nm into the 5-AGNR. The origin of the highly localized

https://doi.org/10.1021/acsnano.4c17602
ACS Nano 2025, 19, 13029−13036

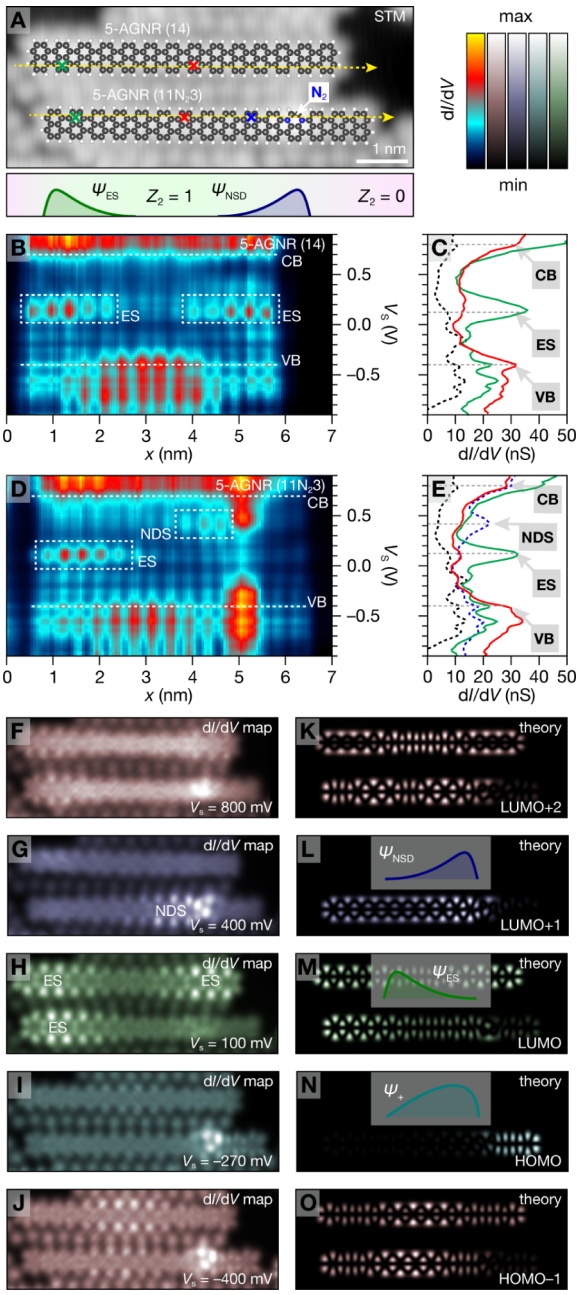

Figure 3. (A) STM topographic image (V_s = −50 mV, I = 150 pA) showing a 5-AGNR(14) and a 5-AGNR(11N$_2$3) (structures overlaid). Sketch indicates the expected positions of the ES and NDS. (B) Line scan STS dI/dV(V_s, x) data acquired on the 5-AGNR(14). ES features are highlighted by dashed rectangles. (C) dI/dV point spectra acquired at the positions marked in (A). (D) Line scan STS dI/dV(V_s, x) data acquired on the 5-AGNR(11N$_2$3). The ES and NDS features are highlighted by dashed rectangles. (E) dI/dV point spectra acquired at the at the positions marked in (A). (F−J) Constant height dI/dV maps acquired on the two GNRs in (A) at the indicated bias voltages. (K−O) Simulated dI/dV maps of the two GNRs in (A) corresponding to the states indicated on the left.

state seen in Figure 3I at V_s = −270 mV associated with the right side of the quinoxaline unit will be addressed below.

Density functional theory calculations (DFT) agree well with the experimental observations. Figure 3K−O shows the predicted local density of states (LDOS) for structures identical to our two experimental GNRs at energies corresponding to the highest occupied molecular orbital − 1 (HOMO − 1), the HOMO, the lowest unoccupied molecular orbital (LUMO), the LUMO + 1 and the LUMO + 2. Simulations were performed for a charge state of q = +2 to account for observed p-doping by the Au(111) surface (both the ES and NDS appear at positive bias and are unoccupied).[47] For the 5-AGNR(14) the LUMO exhibits features typical of ESs (Figure 3M). In the case of the 5-AGNR(3N$_2$11) the LUMO + 1 corresponds to the NDS (Figure 3L) and lies 72 meV above the ES energy. The NDS intensity is seen to gradually decay toward the left. While simulated maps of the NDS and ES show the expected localization at the ends and at the quinoxaline unit (Figure 3L,M), DFT underestimates the extent of the exponential decay of the wave function tail. Similar analysis performed on an even more asymmetric 5-AGNR(17N$_2$1), (Figure S4) shows similar behavior. We conclude from this that dilute N-doped 5-AGNRs feature emergent topological modes at energies corresponding to ε_{ES} = 110 ± 20 meV and ε_{NDS} = 440 ± 40 meV.

Distance-Dependent Hybridization. The STM image of a AGNR(11N$_2$5) and the BRSTM image of a 5-AGNR-(11N$_2$7) can be seen in Figure 4A,D, respectively (structural models are overlaid). When compared to the 5-AGNR(11N$_2$3) of Figure 3, the ES and NDS (Figure 4B,E) are seen to be separated by additional naphthalene units which is expected to lead to weaker hybridization. dI/dV point spectra recorded to the left of the quinoxaline units (red and green lines in Figure 4C,F) are offset relative to the corresponding spectra recorded on the right-hand side (blue lines in Figure 4C,F). While the left side shows the unperturbed NDS and ES at $V_{s(NDS)}$ = 450 mV ($V_{s(NDS)}$ = 387 mV) and $V_{s(ES)}$ = 132 mV ($V_{s(ES)}$ = 117 mV) for 5-AGNR(11N$_2$5) (5-AGNR(11N$_2$7)), the spectra on the right-hand side (blue lines) reveal resonances that are significantly lower in energy than both the NDS and ES. A spectrum acquired on the right-hand side of the 5-AGNR-(11N$_2$5) features a new peak at $V_{s(+)}$ = −97 mV (Figure 4C), whereas a spectrum acquired on the right-hand side of the 5-AGNR(11N$_2$7) features a peak at $V_{s(+)}$ = 1 mV (Figure 4F). Constant height dI/dV maps (using CO-functionalized tips) recorded at V_s = −50 mV and V_s = 0 mV reveal a state extending from the quinoxaline units to the right ends of the 5-AGNR(11N$_2$5) and 5-AGNR(11N$_2$7) (Figure S5). Both the position and relative energies of states localized on the right end of the ribbons are faithfully reproduced by DFT calculations. We conclude that these features represent the bonding linear combination (ψ_+) of the NDS and ES on the right-hand side of both GNRs.

While the NDS and ES remain unperturbed across the N = 11 long naphthalene segment (left side) the shorter N = 5 and N = 7 long naphthalene segments allow for mixing between the NDS and ES which gives rise to hybridized states. Larger overlap along the shorter N = 5 segment lowers the energy of the bonding linear combination compared to the longer N = 7 segment. The stronger hybridization in the 5-AGNR(11N$_2$5) is large enough to lower the state associated with the bonding linear combination below the Fermi level (E_F), thus changing the orbital occupation from vacant to filled on the Au(111) surface. The initial 5-AGNR(11N$_2$3) model system (Figure 3A,D) state at V_s = −270 mV (Figure 3F,I,N) can now be assigned to the bonding linear combination of NDS and ES states hybridizing across the short N = 3 naphthalene segment. The left- and right-sides of dilute N-doped 5-AGNRs can thus

https://doi.org/10.1021/acsnano.4c17602
ACS Nano 2025, 19, 13029−13036

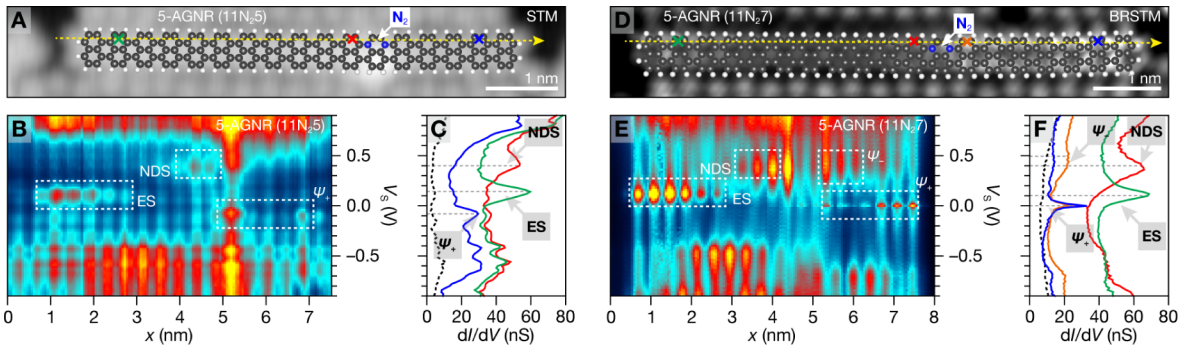

Figure 4. (A) STM topographic image (V_s = −50 mV, I = 150 pA) showing a 5-AGNR(11N$_2$5) (structure overlaid). (B) Line scan STS dI/dV(V_s, x) data acquired on the 5-AGNR(11N$_2$5) in (A). (C) dI/dV point spectra recorded at the positions marked in (A). (D) BRSTM image (constant-height image of current I, V_s = −200 mV) showing a 5-AGNR(11N$_2$7) (structure overlaid). (E) Line scan STS dI/dV(V_s, x) data acquired on the 5-AGNR(11N$_2$7) in (D). (F) dI/dV point spectra recorded at the positions marked in (D).

be considered as largely independent quantum systems, a picture that is further supported by length dependent hybridization in 5-AGNR(7N$_2$5) and 5-AGNR(7N$_2$7) (see Figure S6).

Theoretical Interpretation of Distance Dependence. To shed further light on the hybridization between the NDS and ES we performed DFT simulations on a family of 5-AGNR(1N$_2N$) as a function of the number (N) of naphthalene units to the right of the quinoxaline. Figure 5A shows the frontier state energy levels obtained from DFT, referenced to the midgap energy of the HOMO and LUMO+2 (the states corresponding to the 5-AGNR VB and CB onset). The energies of the LUMO and LUMO + 1 (the bonding and antibonding linear combinations ε_+ and ε_-) are indicated with green and blue crosses, respectively. The energies of the bulk states are shown in red. Orbital plots (LUMO and LUMO + 1) of representative examples for strongly interacting (5-AGNR-(1N$_2$3)) and weakly interacting (5-AGNR(1N$_2$17)) regimes are depicted in Figure 5B. While the 5-AGNR(1N$_2$17) shows the expected unperturbed NDS and ES states, the shorter 5-AGNR(1N$_2$3) shows frontier states that correspond to the linear combinations ψ_+ and ψ_-. The NDS, ES, and linear combinations remain well within the bulk bandgap of the corresponding ribbon segments and their separation converges to $\Delta\varepsilon = \varepsilon_{NDS} - \varepsilon_{ES}$ = 33 meV. Despite notable energy differences, for large N the model qualitatively reproduces the experimentally observed decay of the interaction between NDS and ES with increasing distance toward a finite energy offset. DFT calculations are prone to overestimate the degree of delocalization of wave functions (as reflected in the simulated dI/dV maps of Figures 3 and S5), thus introducing a bias toward long-ranged interaction between NDS and ES.[3,13,50]

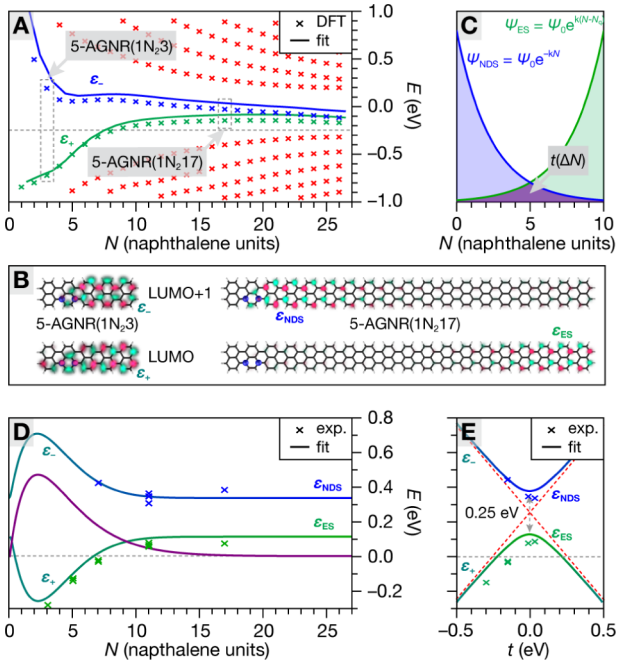

Figure 5. (A) Frontier state energy levels obtained from DFT calculations. (B) DFT calculated LUMO and LUMO + 1 orbitals of a 5-AGNR(1N$_2$3) (left) and LUMO (ES) and LUMO + 1 (NDS) orbitals of a 5-AGNR(1N$_2$17) (right). (C) Empirical model based on exponentially decaying wave functions for the NDS and ES (blue and green lines). Interaction between NDS and ES is approximated by the area of wave function overlap (purple). (D) Experimental data of the bonding (green crosses) and antibonding (blue crosses) state energies of dilute doped N$_2$-5-AGNRs as a function of the distance ΔN between the quinoxaline unit and the ribbon end (blue and green lines are fits of the empirical model, purple line is the calculated function $|t(\Delta N)|$). (E) Interaction diagram showing $\varepsilon_\pm$ (t) for the empirical model.

An instructive description of the interaction can be obtained by turning to an empirical model shown schematically in Figure 5C. Here the wave functions of the NDS and ES are simply assumed to decay exponentially, and the hybridization interaction $t(\Delta N)$ is assumed to be proportional to the overlap between the wave functions (which are separated by ΔN, the number of naphthalene units). An expression for $t(\Delta N)$, can be inserted into eq 2 to derive an analytical expression for the energies of the bonding and antibonding states $\varepsilon_\pm(\Delta N)$ (Supporting Information Discussion 2). Fitting this expression to experimental data (the crosses in Figure 5D) leads to a solution for $\varepsilon_\pm(\Delta N)$ (the green and blue lines in Figure 5D).

The parameters obtained from this fitting procedure (k = 0.45/naphthalene unit) t_0 = 640 meV, $\Delta\varepsilon$ = 250 meV, $\langle\varepsilon\rangle$ = 250 meV, ε_{ES} = 125 meV, and ε_{NDS} = 375 meV were then used to calculate $\varepsilon_\pm$ vs t (see Supporting Information Discussion 2). As shown in Figure 5E this picture qualitatively reproduces the predictions of the dimer Hamiltonian model (solid blue and green lines). The length-dependent interaction between the NDS and ES in 5-AGNRs thus leads to hybridized energy levels tracing out hyperbolae in interaction space (a conic section in (t, $\Delta\varepsilon$, E)-space) that emulate the nondegenerate dimer Hamiltonian introduced in Figure 1B.

https://doi.org/10.1021/acsnano.4c17602
ACS Nano 2025, 19, 13029−13036

CONCLUSIONS

We have shown that the introduction of a substitutional nitrogen dopant along the backbone of a 5-AGNRs causes the emergence of a localized NDS that is offset in energy relative to the native topological ES of the ribbon. For short separation the hybridization between NDS and ES gives rise to a linear combination of polarized states that evolve as a function of effective overlap. Our approach demonstrates new principles for engineering nondegenerate two-site Hamiltonians from basis states formed by two distinct topological interfaces. The introduction of atomically precise nondegenerate localized states, the control over their exchange coupling, and the successful utilization of simple quantum mechanical models provide useful steps toward new designer quantum carbon nanomaterials with potential use in nanoelectronics, photovoltaics, and donor−acceptor applications.

METHODS

Sample Preparation. GNRs were grown on Au(111)/mica films under UHV conditions. Atomically clean Au(111) surfaces were prepared through iterative cycles of Ar^+ ion sputtering and high temperature annealing under UHV conditions. Submonolayer coverages of DIP and DINQ were obtained by sublimation from home-built Knudsen cell evaporators at crucible temperatures of 120−180 °C. Radical step-growth polymerization was achieved by heating the molecule-decorated surface to a temperature of T = 80 °C. Further heating to T = 280 °C for t = 15 min was performed to induce cyclodehydrogenation, which completes the synthesis.

STM Measurements. All STM experiments were performed using a commercial CreaTec LT-STM operating at T = 4 K using tungsten STM tips. STS and dI/dV mapping experiments were all performed under open feedback loop conditions (constant height) using a lock-in amplifier supplying a modulation voltage of V_{ac} = 500 μV (spectroscopy) to V_{ac} = 30 mV (mapping) at a frequency of f = 533 Hz. Tip passivation for dI/dV mapping was achieved by controlled attachment of individual iodine atoms found around the GNRs on the surface. Tip passivation for BRSTM imaging was achieved by controlled attachment of carbon monoxide molecules deposited onto the sample by leaking CO into the STM chamber.[51] Images were processed using WSxM.[52]

Calculations. First-principles calculations were carried out within the density functional theory (DFT) framework, as implemented in the SIESTA package.[53] We adopted the gradient-corrected approximation to the exchange-correlation functional proposed by Perdew, Burke, and Ernzerhof.[54] The Kohn−Sham valence orbitals were expanded in a linear combination of atom-centered basis functions at the double-ζ plus single polarization (DZP) level, in conjunction with a mesh cutoff of 500 Ry. Atomic nuclei and core electrons were represented by norm-conserving pseudopotentials generated according to the Troullier-Martins scheme.[55] The atomic structures were optimized until the maximum component of the force acting on each atom was lower than 0.01 eV/Å. A vacuum region larger than 15 Å was introduced in nonperiodic directions to avoid spurious interactions between periodic replicas. Although we modeled nanoribbons in the gas phase, all our calculations were performed in the 2+ charge state to mimic the charge transfer occurring from the underlying Au(111) substrate in experiments.

ASSOCIATED CONTENT

Supporting Information

The Supporting Information is available free of charge at https://pubs.acs.org/doi/10.1021/acsnano.4c17602.

Topological interpretation of NDS, ES, and hybridized states; STM, BRSTM, STS, and dI/dV maps of dilute N_2-5-AGNRs; analytical model for distance-dependent interaction of NDS and ES (PDF)

AUTHOR INFORMATION

Corresponding Authors

Felix R. Fischer − *Department of Chemistry, University of California, Berkeley, California 94720, United States; Materials Sciences Division, Lawrence Berkeley National Laboratory, Berkeley, California 94720, United States; Kavli Energy NanoSciences Institute at the University of California Berkeley and the Lawrence Berkeley National Laboratory, Berkeley, California 94720, United States; Bakar Institute of Digital Materials for the Planet, Division of Computing, Data Science, and Society, University of California, Berkeley, California 94720, United States;* orcid.org/0000-0003-4723-3111; Email: crommie@berkeley.edu

Michael F. Crommie − *Department of Physics, University of California, Berkeley, California 94720, United States; Materials Sciences Division, Lawrence Berkeley National Laboratory, Berkeley, California 94720, United States; Kavli Energy NanoSciences Institute at the University of California Berkeley and the Lawrence Berkeley National Laboratory, Berkeley, California 94720, United States;* orcid.org/0000-0001-8246-3444; Email: ffischer@berkeley.edu

Authors

Peter H. Jacobse − *Department of Physics, University of California, Berkeley, California 94720, United States;* orcid.org/0000-0002-0777-6050

Michele Pizzochero − *Department of Physics, University of Bath, Bath BA2 7AY, U.K.; School of Engineering and Applied Sciences, Harvard University, Cambridge, Massachusetts 02138, United States;* orcid.org/0000-0003-3948-8202

Ethan Chi Ho Wen − *Department of Chemistry, University of California, Berkeley, California 94720, United States;* orcid.org/0000-0002-8656-5285

Gabriela Borin Barin − *Empa, Swiss Federal Laboratories for Materials Science and Technology, Dübendorf 8600, Switzerland*

Xinheng Li − *Department of Physics, University of California, Berkeley, California 94720, United States*

Zafer Mutlu − *Department of Materials Science and Engineering, University of Arizona, Tucson, Arizona 85719, United States;* orcid.org/0000-0002-2804-8618

Klaus Müllen − *Max Planck Institute for Polymer Research, Mainz D-55128, Germany;* orcid.org/0000-0001-6630-8786

Efthimios Kaxiras − *School of Engineering and Applied Sciences, Harvard University, Cambridge, Massachusetts 02138, United States*

Complete contact information is available at: https://pubs.acs.org/10.1021/acsnano.4c17602

https://doi.org/10.1021/acsnano.4c17602
ACS Nano 2025, 19, 13029−13036

Author Contributions

▲P.H.J., M.P., and E.C.H.W. contributed equally to this work. This research was conceived by P.H.J., Z.M., and G.B.B. Experiments were carried out by P.H.J. under the supervision of M.F.C. Precursor synthesis was performed by E.C.H.W. under the supervision of F.R.F. and K.M. Calculations were performed by M.P. under the supervision of E.K. All authors contributed to the writing and have given approval to the final version of the manuscript.

Notes

The authors declare no competing financial interest.

ACKNOWLEDGMENTS

This work was primarily funded by the US Department of Energy (DOE), Office of Science, Basic Energy Sciences (BES), Materials Sciences and Engineering Division under contract DE-AC02-05-CH11231 (Nanomachine program KC1203) (on-surface growth and STM spectroscopy) and contract DE-SC0023105 (molecular design). Research was also supported by the Office of Naval Research under award N00014-24-1-2134 (molecular synthesis) and N00014-19-1-2596 (topographic analysis). G.B.B. acknowledges the support of the Werner Siemens Foundation (CarboQuant) (molecular characterization). Z.M. acknowledges the support of the National Science Foundation under award CHE-2235143 (molecular deposition). F.R.F. acknowledges generous support from the Heising-Simons Faculty Fellows Program at UC Berkeley (development of synthetic facilities). We thank Dr. Hasan Çelik and the UC Berkeley NMR facility in the College of Chemistry (CoC-NMR) for assistance with spectroscopic characterization. Instruments in the CoC-NMR are supported in part by National Institutes of Health (NIH) award no. S10OD024998.

REFERENCES

(1) Yan, L. H.; Liljeroth, P. Engineered electronic states in atomically precise artificial lattices and graphene nanoribbons. *Adv. Phys-X* **2019**, *4*, 1651672.
(2) Kawai, S.; Nakatsuka, S.; Hatakeyama, T.; Pawlak, R.; Meier, T.; Tracey, J.; Meyer, E.; Foster, A. S. Multiple heteroatom substitution to graphene nanoribbon. *Sci. Adv.* **2018**, *4* (4), No. eaar7181.
(3) Son, Y. W.; Cohen, M. L.; Louie, S. G. Energy gaps in graphene nanoribbons. *Phys. Rev. Lett.* **2006**, *97*, 216803.
(4) Cao, T.; Zhao, F. Z.; Louie, S. G. Topological Phases in Graphene Nanoribbons: Junction States, Spin Centers, and Quantum Spin Chains. *Phys. Rev. Lett.* **2017**, *119*, 076401.
(5) Jiang, J.; Louie, S. G. Topology Classification using Chiral Symmetry and Spin Correlations in Graphene Nanoribbons. *Nano Lett.* **2021**, *21*, 197−202.
(6) Yazyev, O. V. A Guide to the Design of Electronic Properties of Graphene Nanoribbons. *Acc. Chem. Res.* **2013**, *46*, 2319−2328.
(7) Gu, Y. W.; Qiu, Z. J.; Müllen, K. Nanographenes and Graphene Nanoribbons as Multitalents of Present and Future Materials Science. *J. Am. Chem. Soc.* **2022**, *144*, 11499−11524.
(8) Li, J. C.; Sanz, S.; Merino-Díez, N.; Vilas-Varela, M.; Garcia-Lekue, A.; Corso, M.; De Oteyza, D. G.; Frederiksen, T.; Peña, D.; Pascual, J. I. Topological phase transition in chiral graphene nanoribbons: from edge bands to end states. *Nat. Commun.* **2021**, *12* (1), 5538.
(9) Lin, K. S.; Chou, M. Y. Topological Properties of Gapped Graphene Nanoribbons with Spatial Symmetries. *Nano Lett.* **2018**, *18*, 7254−7260.
(10) Anindya, K. N.; Rochefort, A. Spin-Polarized Topological Phases in Graphene Nanoribbons with Non-Benzenoid Defects. *J. Phys. Chem. C* **2023**, *127*, 22856−22864.
(11) Rizzo, D. J.; Veber, G.; Cao, T.; Bronner, C.; Chen, T.; Zhao, F. Z.; Rodriguez, H.; Louie, S. G.; Crommie, M. F.; Fischer, F. R. Topological band engineering of graphene nanoribbons. *Nature* **2018**, *560*, 204−208.
(12) Groning, O.; Wang, S.; Yao, X. L.; Pignedoli, C. A.; Barin, G. B.; Daniels, C.; Cupo, A.; Meunier, V.; Feng, X.; Narita, A.; et al. Engineering of robust topological quantum phases in graphene nanoribbons. *Nature* **2018**, *560*, 209−213.
(13) Rizzo, D. J.; Jiang, J.; Joshi, D.; Veber, G.; Bronner, C.; Durr, R. A.; Jacobse, P. H.; Cao, T.; Kalaylian, A.; Rodriguez, H.; Butler, P.; Chen, T.; Louie, S. G.; Fischer, F. R.; Crommie, M. F. Rationally Designed Topological Quantum Dots in Bottom-Up Graphene Nanoribbons. *ACS Nano* **2021**, *15*, 20633−20642.
(14) Sun, Q.; Yao, X. L.; Groning, O.; Eimre, K.; Pignedoli, C. A.; Mullen, K.; Narita, A.; Fasel, R.; Ruffieux, P. Coupled Spin States in Armchair Graphene Nanoribbons with Asymmetric Zigzag Edge Extensions. *Nano Lett.* **2020**, *20*, 6429−6436.
(15) Rizzo, D. J.; Veber, G.; Jiang, J.; McCurdy, R.; Cao, T.; Bronner, C.; Chen, T.; Louie, S. G.; Fischer, F. R.; Crommie, M. F. Inducing metallicity in graphene nanoribbons via zero-mode superlattices. *Science* **2020**, *369*, 1597−1603.
(16) Sun, Q.; Yan, Y. Y.; Yao, X. L.; Müllen, K.; Narita, A.; Fasel, R.; Ruffieux, P. Evolution of the Topological Energy Band in Graphene Nanoribbons. *J. Phys. Chem. Lett.* **2021**, *12*, 8679−8684.
(17) Slicker, K.; Delgado, A.; Jiang, J. W.; Tang, W. C.; Cronin, A.; Blackwell, R. E.; Louie, S. G.; Fischer, F. R. Engineering Small HOMO-LUMO Gaps in Polycyclic Aromatic Hydrocarbons with Topologically Protected States. *Nano Lett.* **2024**, *24*, 5387−5392.
(18) Mishra, S.; Beyer, D.; Eimre, K.; Kezilebieke, S.; Berger, R.; Groning, O.; Pignedoli, C. A.; Muellen, K.; Liljeroth, P.; Ruffieux, P.; Feng, X. L.; Fasel, R. Topological frustration induces unconventional magnetism in a nanographene. *Nat. Nanotechnol.* **2020**, *15*, 22−28.
(19) Su, W. P.; Schrieffer, J. R.; Heeger, A. J. Solitons in Polyacetylene. *Phys. Rev. Lett.* **1979**, *42*, 1698−1701.
(20) Golor, M.; Koop, C.; Lang, T. C.; Wessel, S.; Schmidt, M. J. Magnetic Correlations in Short and Narrow Graphene Armchair Nanoribbons. *Phys. Rev. Lett.* **2013**, *111*, 85504.
(21) Ortiz, R.; García-Martínez, N. A.; Lado, J. L.; Fernández-Rossier, J. Electrical spin manipulation in graphene nanostructures. *Phys. Rev. B* **2018**, *97*, 195425.
(22) Joost, J. P.; Jauho, A. P.; Bonitz, M. Correlated Topological States in Graphene Nanoribbon Heterostructures. *Nano Lett.* **2019**, *19*, 9045−9050.
(23) Friedrich, N.; Brandimarte, P.; Li, J. C.; Saito, S.; Yamaguchi, S.; Pozo, I.; Pena, D.; Frederiksen, T.; Garcia-Lekue, A.; Sanchez-Portal, D.; Pascual, J. I. Magnetism of Topological Boundary States Induced by Boron Substitution in Graphene Nanoribbons. *Phys. Rev. Lett.* **2020**, *125*, 146801.
(24) Hu, F. M.; Kou, L. Z.; Frauenheim, T. Controllable magnetic correlation between two impurities by spin-orbit coupling in graphene. *Sci. Rep.* **2015**, *5*, 8943.
(25) Gao, F.; Menchon, R. E.; Garcia-Lekue, A.; Brandbyge, M. Tunable spin and conductance in porphyrin-graphene nanoribbon hybrids. *Commun. Phys.* **2023**, *6*, 115.
(26) de Oteyza, D. G.; Frederiksen, T. Carbon-based nanostructures as a versatile platform for tunable π-magnetism. *J. Phys.: Condens. Matter* **2022**, *34*, 443001.
(27) Trainer, D. J.; Srinivasan, S.; Fisher, B. L.; Zhang, Y.; Pfeiffer, C. R.; Hla, S. W.; Darancet, P.; Guisinger, N. P. Artificial Graphene Nanoribbons: A Test Bed for Topology and Low-Dimensional Dirac Physics. *ACS Nano* **2022**, *16*, 16085−16090.
(28) Lado, J. L.; Ortiz, R.; Fernández-Rossier, J. Emergent quantum matter in graphene nanoribbons. In *Graphene Nanoribbons*; IOP: 2020, pp 4-1 to 4-21.
(29) Guo, G.-P.; Lin, Z. R.; Tu, T.; Cao, G.; Li, X. P.; Guo, G. C. Quantum computation with graphene nanoribbon. *New J. Phys.* **2009**, *11*, 123005.
(30) Jacobse, P. H.; Jin, Z.; Jiang, J.; Peurifoy, S.; Yue, Z.; Wang, Z.; Rizzo, D. J.; Louie, S. G.; Nuckolls, C.; Crommie, M. F. Pseudo-

https://doi.org/10.1021/acsnano.4c17602
ACS Nano 2025, 19, 13029−13036

atomic orbital behavior in graphene nanoribbons with four-membered rings. *Sci. Adv.* **2021**, *7*, No. eabl5892.
(31) Pettifor, D. G. The Tight-Binding method: application to AB s-valent dimer. *arXiv*, **2011**. .
(32) Perrin, M. L.; Galan, E.; Eelkema, R.; Grozema, F.; Thijssen, J. M.; van der Zant, H. S. J. Single-Molecule Resonant Tunneling Diode. *J. Phys. Chem. C* **2015**, *119*, 5697−5702.
(33) Xiao, Z. C.; Ma, C.; Huang, J.; Liang, L.; Lu, W.; Hong, K.; Sumpter, B. G.; Li, A.-P.; Bernholc, J. Design of Atomically Precise Nanoscale Negative Differential Resistance Devices. *Adv. Theor. Simul.* **2019**, *2*, 1800172.
(34) Jacobse, P. H.; Kimouche, A.; Gebraad, T.; Ervasti, M. M.; Thijssen, J. M.; Liljeroth, P.; Swart, I. Electronic components embedded in a single graphene nanoribbon. *Nat. Commun.* **2017**, *8*, 119.
(35) Mangnus, M. J. J.; Fischer, F. R.; Crommie, M. F.; Swart, I.; Jacobse, P. H. Charge transport in topological graphene nanoribbons and nanoribbon heterostructures. *Phys. Rev. B* **2022**, *105*, 115424.
(36) Wen, R. L.; Jiang, Z. H.; Miao, R.; Wang, L.; Liang, Y. J.; Deng, J. G.; Shao, Q. Y.; Zhang, J. Electronic transport properties of B/N/P co-doped armchair graphene nanoribbon field effect transistor. *Diamond Relat. Mater.* **2022**, *124*, 108893.
(37) Aviram, A.; Ratner, M. A. Molecular Rectifiers. *Chem. Phys. Lett.* **1974**, *29*, 277−283.
(38) Sekulić, D.; Živanov, M. A Model of the Molecular Rectifying Diode Type Aviram-Ratner. *Electronics* **2010**, *14*, 23−26.
(39) Mesta, M.; Chang, J. H.; Shil, S.; Thygesen, K. S.; Lastra, J. M. G. A Protocol for Fast Prediction of Electronic and Optical Properties of Donor-Acceptor Polymers Using Density Functional Theory and the Tight-Binding Method. *J. Phys. Chem. A* **2019**, *123*, 4980−4989.
(40) Geng, H.; Zhu, L. Y.; Yi, Y. P.; Zhu, D. B.; Shuai, Z. G. Superexchange Induced Charge Transport in Organic Donor-Acceptor Cocrystals and Copolymers: A Theoretical Perspective. *Chem. Mater.* **2019**, *31*, 6424−6434.
(41) Solak, E. K.; Irmak, E. Advances in organic photovoltaic cells: a comprehensive review of materials, technologies, and performance. *RSC Adv.* **2023**, *13*, 12244−12269.
(42) Sisto, T. J.; Zhong, Y.; Zhang, B. Y.; Trinh, M. T.; Miyata, K.; Zhong, X. J.; Zhu, X. Y.; Steigerwald, M. L.; Ng, F.; Nuckolls, C. Long, Atomically Precise Donor-Acceptor Cove-Edge as Electron Acceptors. *J. Am. Chem. Soc.* **2017**, *139*, 5648−5651.
(43) Wen, E. C. H.; Jacobse, P. H.; Jiang, J. W.; Wang, Z. Y.; Louie, S. G.; Crommie, M. F.; Fischer, F. R. Fermi-Level Engineering of Nitrogen Core-Doped Armchair Graphene Nanoribbons. *J. Am. Chem. Soc.* **2023**, *145*, 19338−19346.
(44) Hoffmann, R.; Lipscomb, W. N. Theory of Polyhedral Molecules.1. Physical Factorizations of Secular Equation. *J. Chem. Phys.* **1962**, *36*, 2179−2189.
(45) Longuet-Higgins, H. C. The intersection of potential energy surfaces in polyatomic molecules. *Proc. R. Soc. London A* **1975**, *344*, 147−156.
(46) Liu, R. S. H. Colorful azulene and its equally colorful derivatives. *J. Chem. Educ.* **2002**, *79*, 183−185.
(47) Barin, G. B.; Sun, Q.; Di Giovannantonio, M.; Du, C.-Z.; Wang, X.-Y.; Llinas, J. P.; Mutlu, Z.; Lin, Y. X.; Wilhelm, J.; et al. Growth Optimization and Device Integration of Narrow-Bandgap Graphene Nanoribbons. *Small* **2022**, *18* (31), 2202301.
(48) Song, S. T.; Su, J.; Peng, X. N.; Wu, X. B.; Telychko, M. Recent Advances in Bond-Resolved Scanning Tunneling Microscopy. *Surf. Rev. Lett.* **2021**, *28*, 2140007.
(49) Lawrence, J.; Brandimarte, P.; Berdonces-Layunta, A.; Mohammed, M. S. G.; Grewal, A.; Leon, C. C.; Sanchez-Portal, D.; de Oteyza, D. G. Probing the Magnetism of Topological End States in 5-Armchair Graphene Nanoribbons. *ACS Nano* **2020**, *14*, 4499−4508.
(50) Yang, L.; Park, C.-H.; Son, Y.-W.; Cohen, M. L.; Louie, S. G. Quasiparticle energies and band gaps in graphene nanoribbons. *Phys. Rev. Lett.* **2007**, *99*, 186801.
(51) Bartels, L.; Meyer, G.; Rieder, K. H. Controlled vertical manipulation of single CO molecules with the scanning tunneling microscope: A route to chemical contrast. *Appl. Phys. Lett.* **1997**, *71*, 213−215.
(52) Horcas, I.; Fernandez, R.; Gomez-Rodriguez, J. M.; Colchero, J.; Gomez-Herrero, J.; Baro, A. M. WSXM: A software for scanning probe microscopy and a tool for nanotechnology. *Rev. Sci. Instrum.* **2007**, *78*, 013705.
(53) Soler, J. M.; Artacho, E.; Gale, J. D.; García, A.; Junquera, J.; Ordejón, P.; Sánchez-Portal, D. The SIESTA method for order-N materials simulation. *J. Phys.: Condens. Matter* **2002**, *14*, 2745−2779.
(54) Perdew, J. P.; Burke, K.; Ernzerhof, M. Generalized gradient approximation made simple. *Phys. Rev. Lett.* **1996**, *77*, 3865−3868.
(55) Troullier, N.; Martins, J. L. Efficient Pseudopotentials for Plane-Wave Calculations. *Phys. Rev. B* **1991**, *43*, 1993−2006.

https://doi.org/10.1021/acsnano.4c17602
ACS Nano 2025, 19, 13029−13036